

Anisotropic permeability in deterministic lateral displacement arrays

Rohan Vernekar,^{*a} Timm Krüger,^a Kevin Louthack,^{b‡} Keith Morton^c and David Inglis^d

We investigate anisotropic permeability of microfluidic deterministic lateral displacement (DLD) arrays. A DLD array can achieve high-resolution bimodal size-based separation of micro-particles, including bioparticles such as cells. Correct operation requires that the fluid flow remains at a fixed angle with respect to the periodic obstacle array. We show via experiments and lattice-Boltzmann simulations that subtle array design features cause anisotropic permeability. The anisotropy, which indicates the array's intrinsic tendency to induce an undesired lateral pressure gradient, can lead to off-axis flows and therefore local changes in the critical separation size. Thus, particle trajectories can become unpredictable and the device useless for the desired separation duty. We show that for circular posts the rotated-square layout, unlike the parallelogram layout, does not suffer from anisotropy and is the preferred geometry. Furthermore, anisotropy becomes severe for arrays with unequal axial and lateral gaps between obstacle posts and highly asymmetrical post shapes.

1 Introduction

Deterministic lateral displacement (DLD) is a hydrodynamic size-based particle separation technique capable of high-resolution separation for particles up to five times smaller than the array gap (G in fig. 1(A)). The DLD method can be used with various types of particles and has shown promise in separation and purification of bioparticles¹. This technique employs a periodic obstacle array in a microfluidic channel. The conceptual framework for understanding and designing DLD arrays is based on the assumption that the locally averaged fluid flow direction remains at a fixed angle to the obstacle array. This inclination creates a regular and uniform pattern of fluid flow stagnation streamlines between obstacle posts.

The width of the flow lane created by the first stagnation streamline adjacent to every obstacle determines the critical particle radius r_c ². For a dilute suspension, particles larger than r_c follow the array inclination, and particles smaller than r_c are advected along the fluid streamlines³. In the high Péclet number limit (advection dominating over diffusion), the paths chosen are deterministic. The path for a particle with radius $< r_c$ is called “zigzag” trajectory as the smaller particles move laterally back and forth while following the fluid streamlines. For a particle of

radius $> r_c$ the path is named “bump” trajectory; these particles are bumped into adjacent streamlines by an obstacle post at every row, following the array inclination.

The DLD technique has the advantage of being label-free, relying solely on hydrodynamic and volume exclusion forces to achieve separation. This technique has been demonstrated for various applications such as micro-bead separation^{2,4,5}, fractionation of human blood components^{6–10}, separation of parasites or circulating tumour cells from human blood^{11–13} and deformability-based mapping of human blood^{14–16}. Additionally, various other array post shapes such as square, circular, triangular (right/equilateral), I-shape, L-shape etc. have been employed to obtain improved DLD separation^{17–20}.

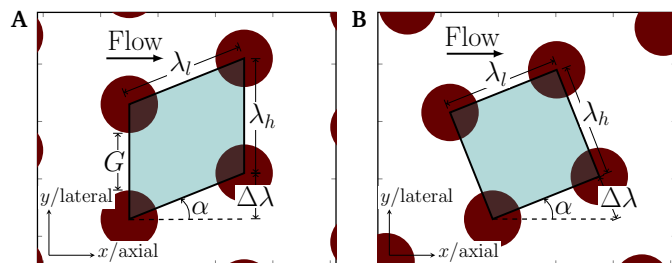


Fig. 1 (A) Row-shifted parallelogram layout and (B) rotated-square layout employed in DLD arrays, with parameters of interest. Note the lateral (up-down) and axial (flow) directions.

Across all published works, posts of any shape are arranged in one of two layouts: row-shifted parallelogram (fig. 1(A)) or rotated-square layout (fig. 1(B)). In the parallelogram layout, adjacent rows of posts are shifted by a fixed amount $\Delta\lambda$, which re-

^a Institute for Materials and Processes, University of Edinburgh, UK. Tel: +44(0)131 6505685; E-mail: R.Vernekar@ed.ac.uk

^b Lawrence Berkeley National Lab, Berkeley, CA, USA.

^c Life Sciences Division, National Research Council of Canada, 75 de Mortagne Boulevard, Boucherville, QC J4B 6Y4, Canada.

^d Department of Engineering, Macquarie University, Sydney, Australia.

[‡] Current address: Berkeley Lights, Inc., Emeryville, CA, USA.

sults in a parallelogram unit cell, and the array has an inclination of $\tan^{-1}(\Delta\lambda/\lambda_h)$ with respect to horizontal flow. In the rotated-square layout, a cartesian periodic array (unit square cell length $\lambda_l = \lambda_h$) is rotated by the required angle $\alpha = \tan^{-1}(\Delta\lambda/\lambda_h)$. Therefore, the ratio $\Delta\lambda/\lambda_h$ determines the array inclination. This quantity is termed row shift fraction ε . When ε is given by 1 over an integer, bi-modal particle separation is expected.

Both parallelogram and rotated-square layouts are equally popular for separation applications; several authors^{6–9,17,18,21–25} have used parallelogram arrays, and others^{4,14,19,20,26,27} have employed the rotated-square layout. Parallelogram arrays are attractive because they have a planar boundary (interface) that is perpendicular to the axial flow direction. This is also an advantage when placing arrays with different separation angles in series (cascaded arrays). However, the significance of the differences between the parallelogram and rotated-square layouts has not been reported so far.

We show that the parallelogram layout, unlike the rotated-square layout, suffers certain drawbacks. These disadvantages include array regions where particle separation does not occur at all, has a different critical size, or even a negative separation angle²². This would lead to particles not separating into distinct bands according to size range and not exiting at the intended outlet ports.

Through extensive lattice-Boltzmann simulations we show that issues with the parallelogram layout arise from array-induced anisotropy. Anisotropy is absent from the rotated-square layout. We also find that anisotropy becomes significant when unequal axial and lateral array gaps are employed and when highly asymmetric post shapes are used. However, this anisotropy only becomes an issue for particle separation when it causes the development of a secondary recirculatory flow. The secondary flow causes a deviation in the flow field such that the flow no longer remains parallel to the side walls everywhere in the device. This leads to a spatially varying critical separation size.

Such secondary recirculation develops when certain design features, which we call “enablers”, are present. We found that an interface gap (before and after array sections) and changing the array angle significantly (e.g. in cascaded devices) act as enablers.

2 Results and Discussion

The aim of this section is to clearly establish the existence of anisotropy and to demonstrate its consequences in DLD arrays. DLD theory^{1,2,4} assumes uniform flow in the direction of the applied pressure gradient. We demonstrate via extensive lattice-Boltzmann simulations that anisotropy can cause the critical radius to change from point to point in a device. Such a variation causes unintended particle trajectories, as observed in our experiments, that are detrimental to deterministic separation. We identify certain design features that enable array anisotropy and can affect the flow field and thence the particle trajectories.

2.1 Anisotropy-induced changes to particle trajectories

Figure 2 shows an image of fluorescent beads flowing through three sections of an array with the row-shifted parallelogram lay-

out (the device is mirrored vertically along the centreline). The beads in this experiment have a radius of $1.0\mu\text{m}$ which is below the expected critical size in all array sections, $r_c = 2.4\mu\text{m}$. The beads should therefore follow the “zigzag” path around array posts and transit the overall device horizontally. However, we see from fig. 2 that while the beads initially track horizontally, the particles begin to mimic a “bump” trajectory as they approach the interface between the first two sections, tracing the local array inclination. In the upper section of the device, particles start to bump upwards at the end of the left array section, then immediately downwards at the start of the middle array section. The particles return to a horizontal trajectory in the middle of the central section before reprising their downward angle as they meet the second interface and finally track upwards again at the start of the right array section.

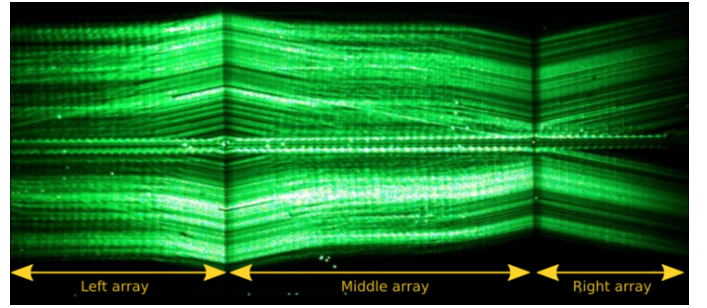


Fig. 2 Fluorescent tracer beads undergo unintended “bump” action near interfaces between array sections in a DLD with three successive parallelogram arrays (circular posts of diameter $7\mu\text{m}$ and a post gap of $4\mu\text{m}$). The device geometry here is also mirrored about the horizontal centreline. The array inclinations (upper section) are $+11.3^\circ$, -11.3° and $+11.3^\circ$ in the left, central and right segments, respectively.

We suspect that this unusual and clearly undesired particle behaviour stems from inherent anisotropic permeability of the parallelogram layout. The average flow direction no longer remains horizontal and tilts in the same direction as the array. As we shall see later with the help of simulations, this flow tilt and the resulting reduction in r_c becomes more pronounced near the interface between array sections. Eventually, when $r_c < 1.0\mu\text{m}$ locally, the $1.0\mu\text{m}$ bead starts to move on the bump mode.

2.2 Nature of array-induced anisotropy

Anisotropic permeability is the tendency of the array to induce a pressure gradient along the lateral axis (vertical in fig. 2). Due to the incompressibility of water, this pressure gradient is only problematic when it induces lateral flow. Figure 2 shows an example of such an anisotropy effect where the flow tilts along the array inclination. The flow tilt reduces the effective array inclination ε locally and therefore also reduces the critical radius r_c . The reduction then causes unexpected particle bumping. To avoid undesired and spatially dependent r_c and unintended particle trajectories, it is crucial to understand and reduce sources of anisotropy.

In 2007, James C. Sturm hypothesised that the parallelogram layout may display greater anisotropy than the rotated layout with a square unit cell²⁸. This hypothesis drew from the understanding of an optical phenomenon known as birefringence²⁹.

Optical birefringence, as seen in materials such as calcite, is caused by anisotropic optical transmission. In calcite it is due to the non-cubic (parallelogram) unit cell. Contrarily, optical materials with cubic unit cells show no anisotropic transmission and no birefringence. The analogy between optics and fluidics serves as a springboard for further investigation into both array layouts that are usually treated as equivalent.

2.3 Mapping anisotropic permeability

We put this hypothesis to the test by using high-resolution lattice-Boltzmann simulations in the Stokes flow limit. Simulations are run in two dimensions and carried out over a single post of the array domain (400×400 lattice cells) with periodic boundary conditions (section 3.1). This approach simulates flow over a central post of an infinite obstacle array. For the purpose of generality, we begin with a symmetric circular post shape with a gap to post diameter ratio (G/D) of unity. The simulated device gap and post diameter are $10\mu\text{m}$ each (post centre-centre distance, $\lambda = 20\mu\text{m}$). Simulations are carried out over the entire range of row shift fraction ($\epsilon = 0.0$ to 1.0 , at 0.1 increments) for both the parallelogram and rotated-square layouts.

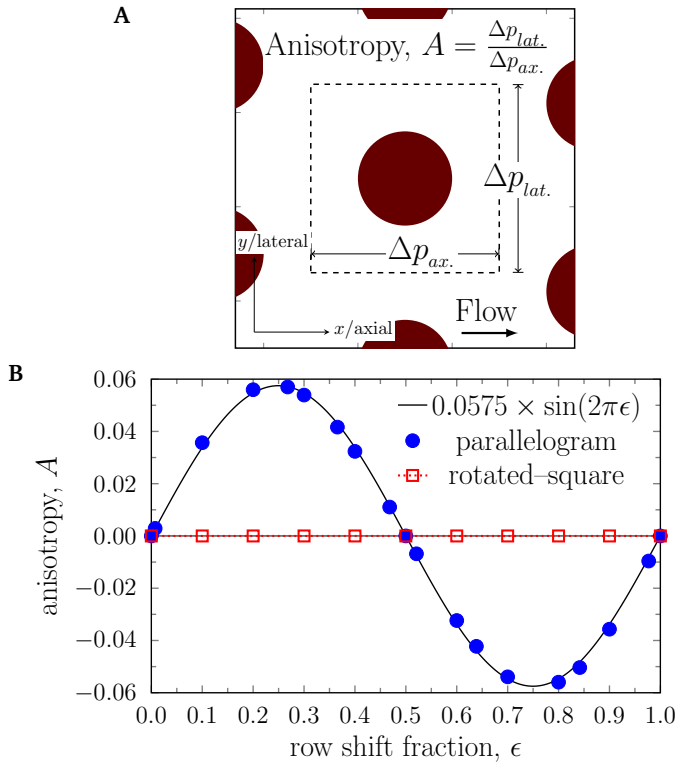


Fig. 3 (A) Definition of anisotropy. Δp is the pressure drop over unit distance for the array. (B) Anisotropy for parallelogram and rotated-square layouts with circular posts for varying array inclination ϵ .

Using periodic boundary conditions to simulate a unit cell (i.e. a single post) of an array possessing anisotropic permeability would result in non-zero average lateral fluid velocity. In real microfluidic devices, this lateral flow is restricted by microchannel side walls. Therefore, we quantify array anisotropy by measuring the lateral pressure drop that is required to maintain zero average

lateral fluid flow. Anisotropy is defined as the dimensionless ratio of the induced lateral pressure gradient to the imposed pressure gradient along the flow direction (fig. 3(A)). Figure 3(B) shows anisotropy values for various inclinations (ϵ) for both the parallelogram and rotated-square layouts. The sign of the anisotropy value indicates the direction of the lateral pressure drop; a positive sign means that the lateral pressure drop is in the same direction as the row shift.

For the parallelogram array, the anisotropy shows a sinusoidal dependence on ϵ . Moreover, the absolute anisotropy values are equal for ϵ and $1 - \epsilon$. This follows from the fact that a parallelogram array with $0.5 < \epsilon < 1.0$ is equivalent to one with $1 - \epsilon$, but with a negative row shift. We observe a maximum anisotropy of $\approx 5.6\%$ occurring at $\epsilon = 0.25$ for the parallelogram array.

The rotated-square layout, however, exhibits vanishing anisotropy for all tested values of ϵ . This substantiates the hypothesis of the rotated-square layout having an advantage over the parallelogram layout in avoiding anisotropic effects.

2.4 Anisotropy-induced flow tilt

Array anisotropy can only affect particle trajectories when it causes a tilt in the flow direction. For the parallelogram layout with symmetric circular posts, the direction of anisotropy is the same as the row shift. Therefore, anisotropic flow tilt is towards the array incline and causes a decrease in the effective array inclination.

To demonstrate the reduction of the effective inclination, we simulated the mid-section of two DLD devices, one with the parallelogram layout (fig. 4(A)) and the other with the rotated-square layout (fig. 4(B)). Each device has 152 circular posts along the flow and 120 posts along the transverse direction. The post diameter is $10\mu\text{m}$, and the gap between posts is $10\mu\text{m}$. The simulated domain is $3.2\text{mm} \times 2.4\text{mm}$ (3200×2400 lattice cells) with periodic inlet and outlet flow conditions (fig. 4). The flow is driven by a pressure gradient along the axial direction. Each device has two array sections with alternating array inclinations. The left section has a positive array inclination of $\epsilon = 0.2$, the right section an inclination $\epsilon = -0.2$. Both sections are separated by a gap of ≈ 4 posts ($80\mu\text{m}$). Streamlines (blue lines) are shown in the zoomed sections (right panels in fig. 4(A) and (B)) for both devices, along with velocity vectors.

In the parallelogram device (fig. 4(A)), the streamline near the bottom wall remains horizontal throughout. As we move away from the bottom wall toward the centre of the device, the streamlines start tilting along the prevalent array inclination. Already ten posts away from the bottom wall, this effect becomes important. The tilt continues to increase as we move further away from the bottom wall. In the central region of the device (typically the particle separation zone), the flow is no longer parallel to the side walls of the device. We also observe a similar behaviour at the top wall (data not shown).

At the centre of this simulation, the effective array inclination is reduced from $1/5$ to $\approx 1/6.8$. This change in ϵ occurs gradually with position and is therefore rarely one over an integer. It is known that such non-integer periodicity values for bump ar-

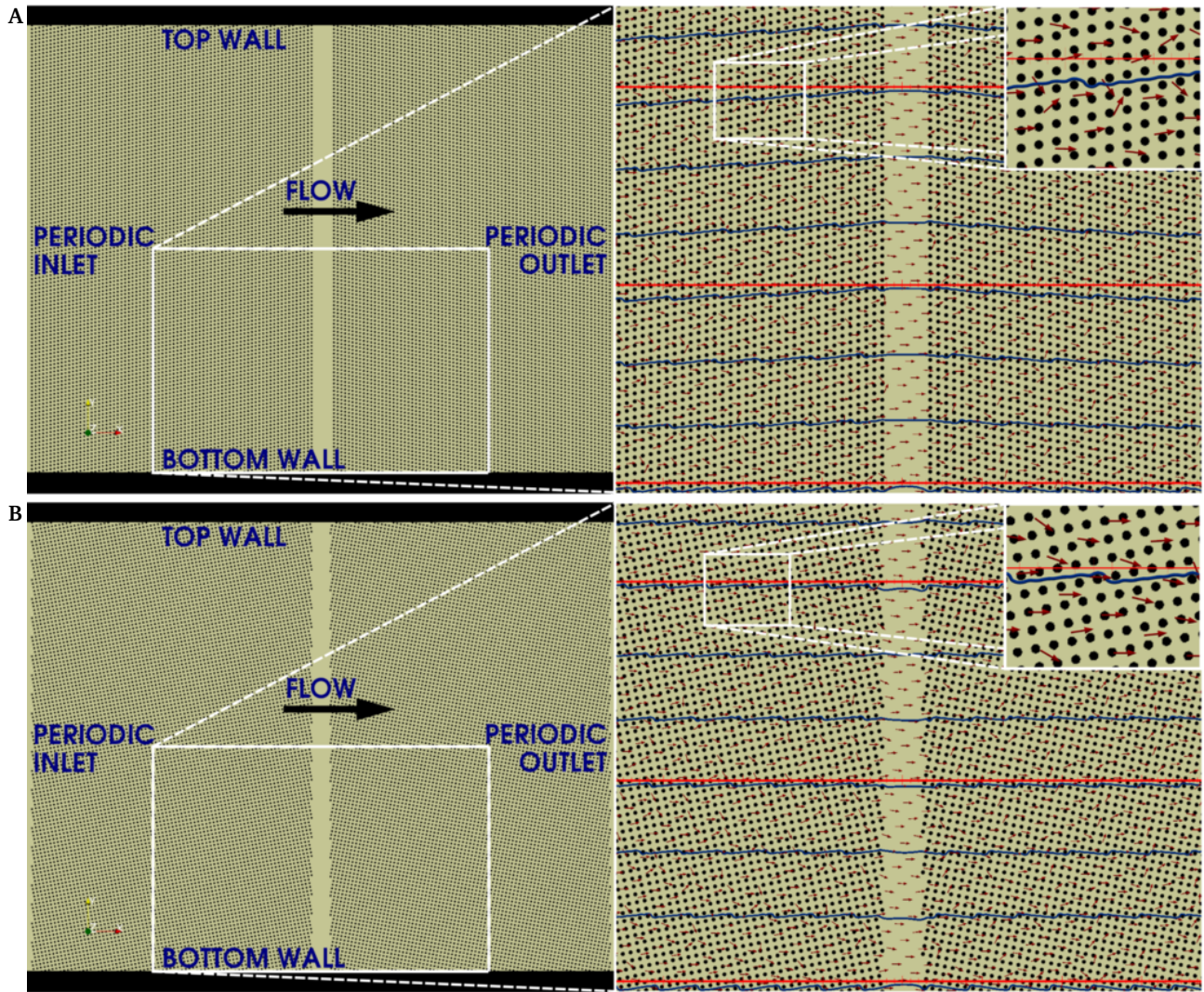


Fig. 4 Fluid streamlines (blue) in (A) parallelogram and (B) rotated-square layout devices. Reference horizontal lines in the left panels (red) correspond to the applied pressure drop direction (parallel to side walls). The streamlines are tilted in the parallelogram layout device, whereas the streamlines remain parallel to the applied pressure drop and follow the “zigzag” path in the rotated-square layout device. The small deviations (“zigzag”) from the horizontal line in the latter case are due to the streamlines navigating around posts.

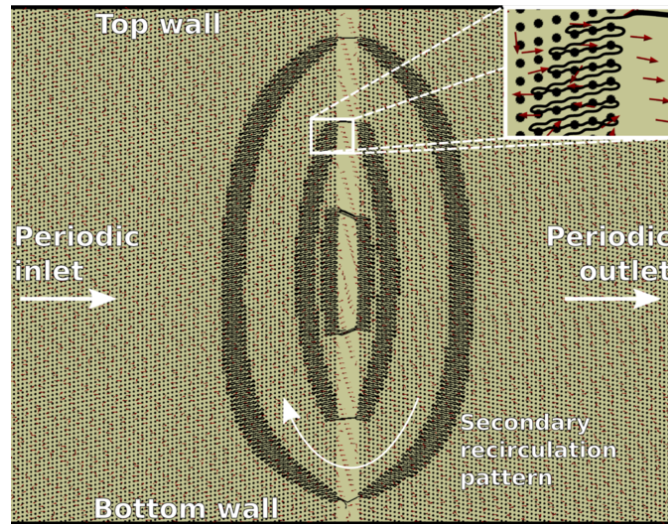


Fig. 5 Secondary recirculation flow pattern in the parallelogram device (fig. 4A) obtained by subtracting the x -component of the primary velocity measured at the device centre from the overall velocity field.

rays can cause multi-directional sorting modes as well as negative directional locking^{22,26}. All of these effects are highly undesirable for deterministic bimodal particle sorting. Furthermore, secondary factors, such as the distance from the side walls, now influence the critical radius.

In the rotated-square device (fig. 4(B)), the streamlines (blue lines) are horizontal. The streamlines remain on their predicted course (“zigzag” around the the posts), parallel to the side walls of the device. This can be attributed to the absence of anisotropy. Unlike the parallelogram layout, use of the rotated-square array leads to a well-defined and constant critical radius throughout the device. Therefore, the rotated-square layout should be preferred for particle separation applications.

2.5 Secondary recirculation flow

We have seen that inherent anisotropic permeability of the parallelogram layout can tilt the streamlines away from the side walls, along the prevalent array inclination. However, as has been demonstrated in the literature, this need not always be the case. Under some conditions, the array anisotropy leads to a lateral pressure gradient that is balanced by normal stresses at the side walls. In this case, the streamlines are not tilted and particle trajectories are not affected. As we shall see later, certain DLD design features, however, allow the lateral pressure gradient to induce secondary flows that tilt the streamlines.

Investigating the flow field in fig. 4(A), we find that the anisotropic lateral pressure drop gets released near the array section interface manifesting as a secondary recirculation in the device. We plot this complex recirculation pattern in fig. 5. The secondary flow field is obtained by subtracting the axial velocity component at the centre of the device ($1.6\text{mm}, 1.2\text{mm}$) from the overall velocity field. The circulation is clockwise in this case, and meanders around the posts in the array. The recirculatory flow causes the streamline tilt which in turn alters the critical radius locally. We find that the recirculatory flow is absent when the rotated-square layout is used. As demonstrated next, secondary recirculatory flow manifests when certain device design features, “enablers”, are present in devices with intrinsic anisotropy.

2.6 Anisotropic secondary flow enablers

Certain design features that allow the anisotropic pressure gradient to drive the recirculatory flow are quite common in DLD devices. In general, placing arrays with opposing anisotropy values next to each other (as done in fig. 2 and 4) allows the secondary background flow to develop. Also having sections with significant difference in anisotropy value as well as a low-impedance isotropic zone, such as an interface gap between array sections, can lead to recirculation.

To demonstrate the effect of an interface gap between device section, we carried out two simulations with the anisotropic parallelogram array with $\varepsilon = 0.25$. One device features an interface gap between sections (fig. 6(A)), while the other does not (fig. 6(B)). The interface section gap acts as an enabler by allowing the fluid flux to compensate for its upward anisotropic tilt in the arrays (fig. 6(A)). The gap permits the development

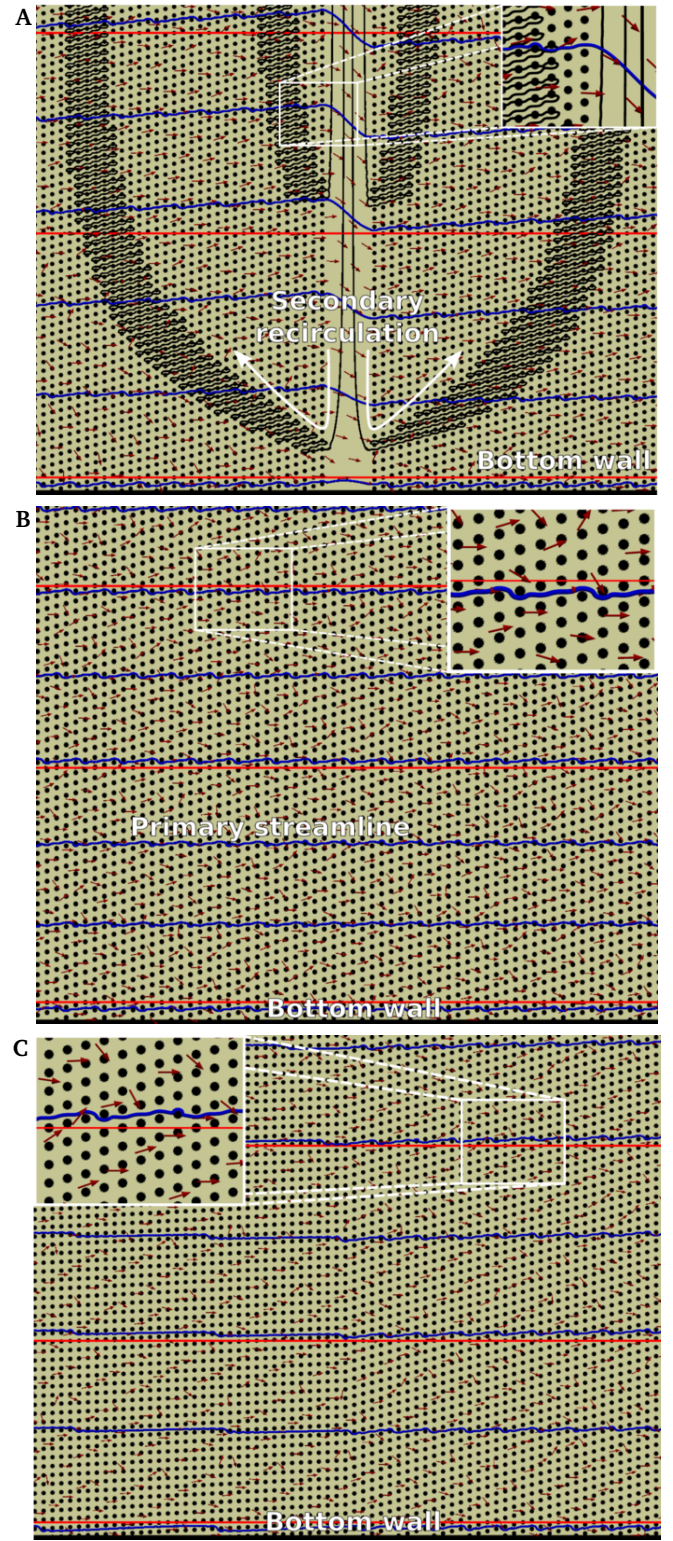


Fig. 6 Fluid streamlines (blue) in a DLD device (A) with interface gap and (B) without gap between successive array sections. The device has a parallelogram layout with circular posts and $\varepsilon = 0.25$ in both sections. In (A) the secondary flow pattern is visualised in black. (C) Streamlines in a cascaded DLD with $\varepsilon = 0.05$ (left section) and $\varepsilon = 0.25$ (right section). Horizontal lines (red) indicate the applied pressure gradient direction. All panels are zoomed-in views, taken near the bottom side wall, of larger devices.

of two counter-rotating secondary recirculations (black lines in fig. 6(A)). In the absence of the gap, the flow remains horizontal everywhere (fig. 6(B)).

Even without an interface gap, the anisotropic flow tilt manifests when two array sections with significant differences in anisotropy are used next to one another (cascaded array). We carried out a simulation of a cascaded design with the left array section (parallelogram) at $\epsilon = 0.05$ and the right array section (parallelogram) at $\epsilon = 0.25$, without an interface gap in between (fig. 6(C)). The array section with higher anisotropy dominates and causes complementary flow tilts in the adjacent array sections. Figure 6(C) shows that the flow tilts slightly upwards in the right array section ($\epsilon = 0.25$) and, in order to compensate for this tilt, slightly downwards in the left array ($\epsilon = 0.05$), away from the side walls. Here the effective array inclinations (in the central simulation zone) become $\epsilon = 0.231$ and $\epsilon = 0.068$ in the right and left sections respectively. We therefore find that a cascaded parallelogram array may generally have a locally varying critical radius r_c .

An interface gap is often seen at the beginning and the end of arrays in most DLD devices. These gaps should be avoided. The cascaded arrangement for arrays is commonly employed for separation of more than two particle species in a single device. In such applications, the rotated-square layout should be used in cascade, rather than the parallelogram layout. In principle, it is possible to suppress all lateral flow by enforcing uniform mass flow along the entrance and exit to an array. This is easily done in simulations but to do so in practice would require a large number of high-impedance channels to feed and collect fluid. Furthermore, to be effective the impedance of these channels must be comparable to the impedance of the entire array. This is often not possible in a device that must meet constraints on device area, throughput, and shear stress. Therefore, as a general rule, interface gaps at the start/end or between DLD array sections should be avoided and the rotated-square layout favoured.

2.7 Causes of increased anisotropic permeability

We investigate further design features that cause anisotropy, including the array gap aspect ratio and the pillar shape.

2.7.1 Effect of unequal axial to lateral post distance

DLD devices with unequal axial and lateral gaps between posts have been shown to give enhanced separation in specific applications^{6,30}. Using such non-unity aspect ratios for the array unit cells clearly has value, but we show here that there is a cost in terms of higher anisotropy. As previously, we carry out single post simulations to study the effect of gap aspect ratio on array anisotropy. The aspect ratio is quantified as $AR = \lambda_l/\lambda_h$ (fig. 1(A) and (B)). Here we vary the axial gap λ_l ; the lateral gap and pillar diameter are both kept equal to $G = D = \lambda_h/2$. All other simulation parameters are the same as before.

Figure 7(A) shows the variation of anisotropy at array inclinations of $\epsilon = 0.1, 0.3, 0.5, 0.7, 0.9$ for the parallelogram array. The cases $\epsilon = 0.3, 0.7$ and $\epsilon = 0.1, 0.9$ are equivalent, respectively, except for the direction of array inclination. Therefore, their anisotropy curves are mirror-symmetric about the x -axis. For

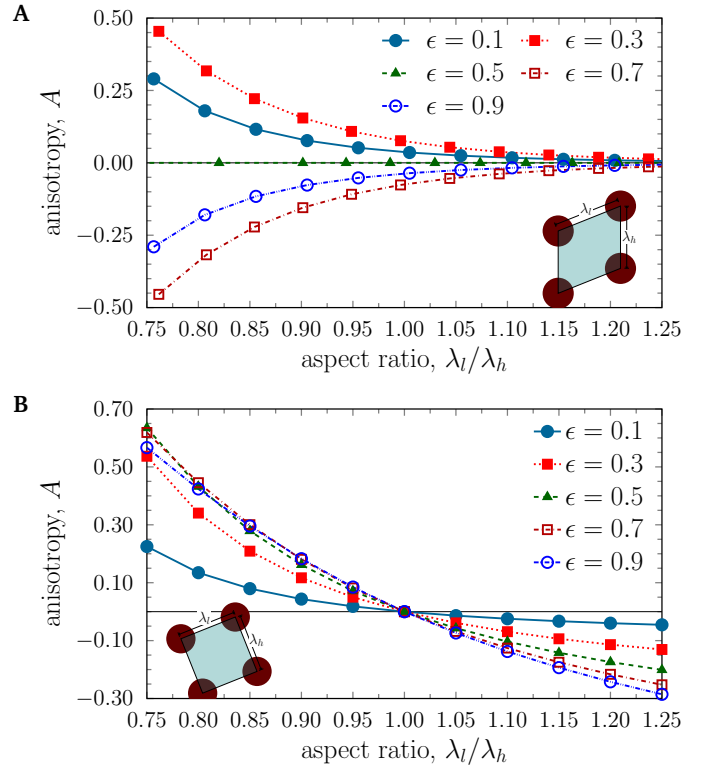


Fig. 7 Variation of anisotropy with aspect ratio of the unit cell for the (A) parallelogram and the (B) rotated-square layout.

$\epsilon = 0.5$, the anisotropy must vanish for all aspect ratios due to symmetry reasons.

Interestingly, in the parallelogram array, the anisotropy steadily decreases and converges to zero with increasing AR or λ_l . This is an important result for reducing the anisotropic permeability in parallelogram arrays, especially since the critical radius r_c is independent of the aspect ratio, at constant ϵ (our simulations predict r_c to be $1.8\mu\text{m}$ for $\epsilon = 0.1$ and $3.6\mu\text{m}$ for $\epsilon = 0.3$, independent of the aspect ratio). However, $AR > 1$ has a clear disadvantage; large aspect ratios mean longer devices for the same lateral displacement. This raises issues of greater device footprints and higher fluidic resistance. Therefore such arrays are not common.

Figure 7(B) shows the anisotropy values for inclinations $\epsilon = 0.1, 0.3, 0.5, 0.7, 0.9$ for the rotated-square array. Unlike in the parallelogram array, the arrays with $\epsilon = 0.1, 0.9$ and $\epsilon = 0.3, 0.7$, respectively, are no longer equivalent for $AR \neq 1$. This indicates that the critical diameter in rotated-square arrays is a function of AR , even for fixed inclination α . We observe that the sign of the anisotropy changes when the aspect ratio crosses the value 1. For $AR < 1$ the anisotropy is positive, for $AR > 1$ it is negative. $AR = 1$ leads to zero anisotropy for all investigated values of ϵ . This is an important result; unless other requirements call for non-unity aspect ratios in rotated-square arrays, $AR = 1$ should be chosen. If the aspect ratio is not unity, the anisotropy can be reduced by decreasing ϵ .

2.7.2 Post shape induced anisotropy

We find that anisotropy becomes severe when asymmetric post shapes are used. Figure 8 displays images from an experiment with right-triangular posts arranged in the rotated-square layout with negative array inclination ($\epsilon = -0.1$). Figure 8(A) shows the interface gap between two array sections with larger cylindrical pillars (roof supports) placed in the gap. All array parameters are equal in both the left and right sections ($6\mu\text{m}$ post size, $4\mu\text{m}$ gap, row shift fraction $\epsilon = -1/10$). However, the right-triangular posts are rotated by 90° counter-clockwise in the right array section relative to those in the left array section.

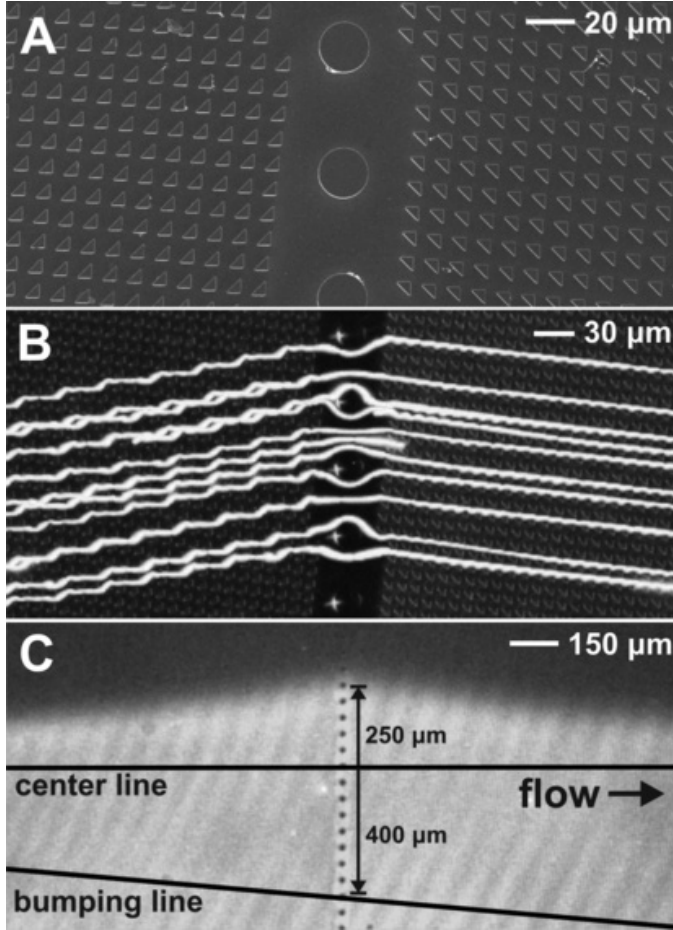


Fig. 8 Experimental device using right-triangular posts with rotated-square layout. (A) Scanning electron micrograph of the junction between two array sections. The array inclination is identical on either side ($\epsilon = -0.1$), but the triangular posts are rotated. (B) Epifluorescence micrograph showing trajectories of super-critical $3.1\mu\text{m}$ diameter fluorescent beads. In the left section the beads are in the zigzag mode, while in the right section they travel in the bump mode. (C) Fluorescent dye is injected along the bottom wall of the device. The dye deviates upwards in the left section and downwards in the right section. This indicates anisotropic flow in both array sections.

Figure 8(B) shows the trajectories of fluorescent beads with $3.1\mu\text{m}$ diameter which is greater than the design critical radius ($r_c = 1.1\mu\text{m}$ on the vertex side and $r_c = 1.5\mu\text{m}$ on the flat side of the triangle). Therefore, the beads should follow the bump trajectory moving downwards along the array inclination. Instead we

can see that the beads move along an abnormal “zigzag” trajectory in the left array section. However, in the right array section, the same beads start following the “bump” trajectory. Close to the central interface gap, the beads bump on the flat side of the right triangular posts, rather than on the vertex side as was intended. This unexpected behaviour is due to anisotropic flow induced in the device caused by the strongly anisotropic post shape, as we will demonstrate in the following. It appears that the flow pattern in both sections tilts along the hypotenuse of the triangle, thereby increasing the effective negative inclination in the left section and decreasing it in the right section. In fact, particles bumping on the flat side of the triangles in the right section indicate that the flow tilts beyond $\alpha = \tan^{-1}(\epsilon) = -5.7^\circ$, effectively creating a positively inclined array region close to the central interface gap.

To visualise the streamline tilt, fluorescent dye was introduced in the bottom section of the DLD (fig. 8(C)). The local deviation of the flow is marked out by the interface between the dye and non-dye regions. This clearly reveals that the inclination of the flow is no longer horizontal and aligns with the hypotenuse of the triangular posts in the array segments. We see that away from the side walls, the flow deviates by as much as $\approx 250\mu\text{m}$, from the horizontal. Such large deviation arising from the anisotropic pillar shape therefore induces completely opposite particle behaviour than intended.

2.7.3 Measuring flow inclination

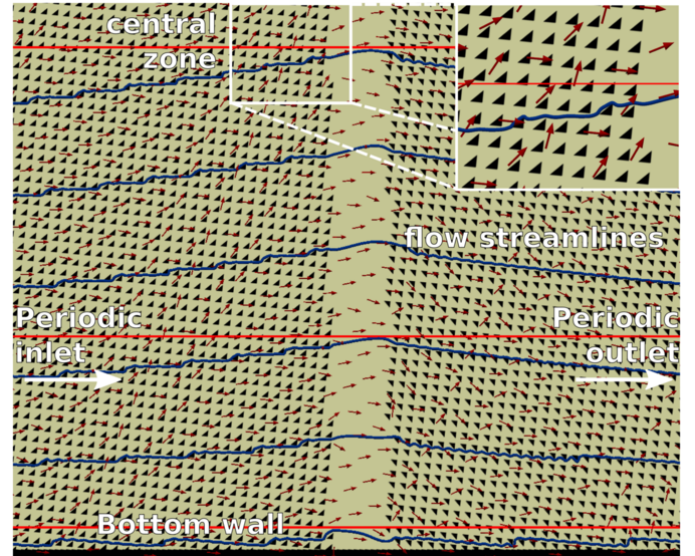







Fig. 9 Streamlines (blue) in a simulated device similar to the experimental one in fig. 8. Away from the bottom wall, the streamlines deviate significantly from the horizontal due to array anisotropy. The reference horizontal line (red) gives the applied pressure gradient direction.

To measure the extent of the streamline tilt, we simulated a device with 152×103 triangular posts along the flow and transverse directions, respectively. The inclination is $\epsilon = -0.1$ and the device parameters match those in the experiment ($6\mu\text{m}$ post size, $4\mu\text{m}$ gap). The boundary conditions for the simulated device (3200×2400 lattice cells) are the same as those for devices shown in fig. 4. In particular, the simulation domain has two ar-

ray sections, with the triangular posts in the right section rotated by 90° relative to those in the left section. The central interface gap is $\approx 50\mu\text{m}$ and simulated without the cylindrical roof supports (fig. 9).

Figure 9 shows a subset of the simulation domain at the bottom wall. We plot the streamlines (blue lines) along with the fluid velocity vectors. The horizontal (red) lines indicate the direction of the applied pressure gradient. We can see that, at around ten posts away from the bottom wall, the flow tilts significantly along the triangle post hypotenuse. The tilt increases to a maximum as we move towards the centre of the device. We approximate the flow tilt in the central zone, near the central interface gap, by averaging over six equi-spaced streamlines (figure not shown). For the left array section with the triangles pointing up, the flow tilts by $\approx +11.3^\circ$. This would correspond to an effective array inclination of $\varepsilon \approx -0.31$ and an estimated (using parabolic flow theory²) critical radius of $\approx 1.48\mu\text{m}$. In the right array section with the triangular posts pointing down, we measure the tilt to be $\approx -11.9^\circ$ and therefore an effective array inclination of $\varepsilon \approx +0.11$ and an estimated critical radius of $\approx 0.825\mu\text{m}$. These results support the experimental observations of having particles of radius $1.55\mu\text{m}$ in the “zigzag” mode in the left section and in the “bump” mode in the right section.

Table 1 Anisotropy for different post shapes in the rotated-square layout with an inclination of $\varepsilon = 0.1$. The finite anisotropy for the circular post ($O(10^{-7})$) is caused by numerical approximations. Note that anisotropy for the parallelogram layout array with circular posts at $\varepsilon = 0.1$ is 3.6×10^{-2} .

| Post shape | | Anisotropy, A |
|----------------------|---|----------------------|
| Circular |  | 3.1×10^{-7} |
| Square |  | 2.1×10^{-6} |
| Equilateral triangle |  | 3.2×10^{-3} |
| Right triangle |  | 1.8×10^{-1} |
| I-shape |  | 5.2×10^{-3} |

2.7.4 Anisotropy of non-circular posts

To understand the role of the pillar shape better, we simulated a single post with periodic boundary conditions (400×400 lattice cells) and measured the anisotropy for different post shapes commonly employed in DLD devices. We tested the square¹⁷, equilateral triangle^{13,20}, right triangle¹⁹ and I-shape^{17,18} posts in a rotated-square layout for an inclination of $\varepsilon = 0.1$. These posts are defined such that they can be inscribed in a circle of diameter $10\mu\text{m}$. Each post is rotated to align with the array inclination at $\varepsilon = 0.1$. The results are collected in table 1, along with those for the circular post ($10\mu\text{m}$ diameter). We see that highly asymmetric post shapes, such as the right triangle, display anisotropy an order of magnitude higher than the maximum due to parallelogram layout with circular posts. However, the anisotropy of other post shapes is close to zero and lower than that of the parallelogram layout with cylindrical posts. Therefore, the anisotropy caused by

the device layout can be more important than the post-induced anisotropy, and the rotated-square layout is generally preferable.

3 Materials and Method

3.1 Simulation details

The simulations were carried out using our validated lattice-Boltzmann code³¹. The no-slip wall boundary condition is implemented using the standard half-way bounce-back model. The relaxation time is set to unity with the standard BGK collision operator. All the simulations are in the Stokes flow regime with Reynolds number (computed based on maximum velocity and array gap, G) of $Re < 0.8$ for the single post simulations and $Re < 1 \times 10^{-4}$ for the large domain simulations.

3.2 Experimental procedure

Microfluidic devices used in this work were fabricated by standard photolithographic techniques and deep reactive ion etching as described in²³. Approximately 1 mm diameter through holes were sand-blasted using a dental sand blaster. Devices were sealed using a large PDMS coated glass coverslip, and wet by immersion in water containing 2g/L pluronic F108 (BASF), as detailed in³². Fluorescent polystyrene beads were diluted into ultrapure water containing 2g/L F108 and thoroughly sonicated to break up aggregates prior to being introduced into the devices.

4 Conclusion

Via experiments and lattice-Boltzmann simulations we investigated anisotropic permeability of deterministic lateral displacement (DLD) arrays. Anisotropic devices induce a pressure gradient perpendicular to the axial flow direction. DLD anisotropy can manifest as undesired localised secondary flows (e.g. recirculation patterns). Secondary flows are undesired as they cause the imposed flow to tilt away from its intended axial direction, which in turn leads to a locally varying critical separation size and unintended particle trajectories.

We found that the parallelogram layout displays inherent anisotropy that grows with increasing array inclination with respect to the axial flow ($0 < \varepsilon \leq 0.25$). Contrarily, the rotated-square layout with circular posts shows no anisotropy and therefore no flow tilt. Hence, in the rotated-square array, the flow remains parallel to the side walls throughout, and the critical radius is predictable. We can thus recommend the rotated-square layout, rather than the parallelogram layout.

Also non-equal axial and lateral post gaps and non-circular post shapes can lead to array anisotropy, even for the rotated-square layout. While square, equilateral triangle and I-shaped pillars lead to a relatively low anisotropy, right triangle posts cause a large anisotropy that can lead to significant streamline tilt.

If anisotropic arrays are used, one should avoid “enabler” design features that allow the anisotropy to trigger off-axis secondary flows. One typical enabler feature is the interface gap between array segments in cascaded DLD devices.

Anisotropic permeability plays an important role in determining the success or failure of a DLD device and needs to be accounted for while designing such separation arrays.

5 Acknowledgements

D. Inglis would like to thank James C. Sturm for suggesting the optical birefringence analogy, the inspiration for this work, way back in 2007. T. Krüger would like to thank the University of Edinburgh for the award of a Chancellor's Fellowship and full funding of this work.

References

- 1 J. McGrath, M. Jimenez and H. Bridle, *Lab Chip*, 2014, **14**, 4139–4158.
- 2 D. W. Inglis, J. A. Davis, R. H. Austin and J. C. Sturm, *Lab on a Chip*, 2006, **6**, 655–658.
- 3 R. Vernekar and T. Krüger, *Medical Engineering & Physics*, 2015, **37**, 845–854.
- 4 L. R. Huang, E. C. Cox, R. H. Austin and J. C. Sturm, *Science*, 2004, **304**, 987–990.
- 5 T. Kulrattanarak, R. G. M. v. d. Sman, C. G. P. H. Schroën and R. M. Boom, *Microfluidics and Nanofluidics*, 2010, **10**, 843–853.
- 6 J. A. Davis, D. W. Inglis, K. J. Morton, D. A. Lawrence, L. R. Huang, S. Y. Chou, J. C. Sturm and R. H. Austin, *Proceedings of the National Academy of Sciences*, 2006, **103**, 14779–14784.
- 7 D. W. Inglis, M. Lord and R. E. Nordon, *Journal of Micromechanics and Microengineering*, 2011, **21**, 054024.
- 8 D. W. Inglis, K. J. Morton, J. A. Davis, T. J. Zieziulewicz, D. A. Lawrence, R. H. Austin and J. C. Sturm, *Lab on a Chip*, 2008, **8**, 925–931.
- 9 S. Zheng, R. Yung, Y.-C. Tai and H. Kasdan, 18th IEEE International Conference on Micro Electro Mechanical Systems, 2005. MEMS 2005, 2005, pp. 851–854.
- 10 N. Li, D. Kamei and C.-M. Ho, 2nd IEEE International Conference on Nano/Micro Engineered and Molecular Systems, 2007. NEMS '07, 2007, pp. 932–936.
- 11 S. H. Holm, J. P. Beech, M. P. Barrett and J. O. Tegenfeldt, *Lab on a Chip*, 2011, **11**, 1326–1332.
- 12 K. Loutharback, J. D'Silva, L. Liu, A. Wu, R. H. Austin and J. C. Sturm, *AIP Advances*, 2012, **2**, year.
- 13 Z. Liu, F. Huang, J. Du, W. Shu, H. Feng, X. Xu and Y. Chen, *Biomicrofluidics*, 2013, **7**, 011801.
- 14 J. P. Beech, S. H. Holm, K. Adolfsson and J. O. Tegenfeldt, *Lab on a Chip*, 2012, **12**, 1048–1051.
- 15 D. Holmes, G. Whyte, J. Bailey, N. Vergara-Irigaray, A. Ekpenyong, J. Guck and T. Duke, *Interface Focus*, 2014, **4**, 20140011.
- 16 E. Henry, S. H. Holm, Z. Zhang, J. P. Beech, J. O. Tegenfeldt, D. A. Fedosov and G. Gompfer, *Scientific Reports*, 2016, **6**, 34375.
- 17 K. K. Zeming, S. Ranjan and Y. Zhang, *Nature Communications*, 2013, **4**, 1625.
- 18 S. Ranjan, K. K. Zeming, R. Jureen, D. Fisher and Y. Zhang, *Lab on a Chip*, 2014, **14**, 4250–4262.
- 19 K. Loutharback, J. Puchalla, R. H. Austin and J. C. Sturm, *Physical Review Letters*, 2009, **102**, 045301.
- 20 K. Loutharback, K. S. Chou, J. Newman, J. Puchalla, R. H. Austin and J. C. Sturm, *Microfluidics and Nanofluidics*, 2010, **9**, 1143–1149.
- 21 R. Huang, T. A. Barber, M. A. Schmidt, R. G. Tompkins, M. Toner, D. W. Bianchi, R. Kapur and W. L. Flejter, *Prenatal Diagnosis*, 2008, **28**, 892–899.
- 22 B. R. Long, M. Heller, J. P. Beech, H. Linke, H. Bruus and J. O. Tegenfeldt, *Physical Review E*, 2008, **78**, 046304.
- 23 K. J. Morton, K. Loutharback, D. W. Inglis, O. K. Tsui, J. C. Sturm, S. Y. Chou and R. H. Austin, *Proceedings of the National Academy of Sciences*, 2008, **105**, 7434–7438.
- 24 R. Quek, D. V. Le and K.-H. Chiam, *Physical Review E*, 2011, **83**, 056301.
- 25 H. N. Joensson, M. Uhlén and H. A. Svahn, *Lab on a Chip*, 2011, **11**, 1305–1310.
- 26 M. Balvin, E. Sohn, T. Iracki, G. Drazer and J. Frechette, *Physical Review Letters*, 2009, **103**, 078301.
- 27 D. W. Inglis, N. Herman and G. Vesey, *Biomicrofluidics*, 2010, **4**, 024109.
- 28 J. Sturm, *Private correspondence to Dr. D. Inglis*, 2007.
- 29 E. Hecht, *Optics*, Addison-Wesley, 2002.
- 30 K. K. Zeming, T. Salafi, C.-H. Chen and Y. Zhang, *Scientific Reports*, 2016, **6**, 22934.
- 31 T. Krüger, D. Holmes and P. V. Coveney, *Biomicrofluidics*, 2014, **8**, 054114.
- 32 R. S. Pawell, D. W. Inglis, T. J. Barber and R. A. Taylor, *Biomicrofluidics*, 2013, **7**, 056501.